PHYSICAL REVIEW B **69**, 035314 (2004)

Laser-generated nonlinear surface wave pulses in silicon crystals

A. M. Lomonosov and P. Hess
Institute of Physical Chemistry, University of Heidelberg, Im Neuenheimer Feld 253, 69120 Heidelberg, Germany

R. E. Kumon* and M. F. Hamilton
Department of Mechanical Engineering, The University of Texas at Austin, Austin, Texas 78712-0292, USA

(Received 25 July 2003; revised manuscript received 7 October 2003; published 22 January 2004)

The absorption-layer method for inducing pressure shocks is employed to generate finite-amplitude, broadband surface wave pulses in crystalline silicon. Spectral evolution equations are used to compute the wave form distortion from the first to the second measurement location, and the results are shown to be in quantitative agreement with the measured data. The measurements also confirm that a nonlinearity matrix which describes the coupling of harmonics provides a useful tool for characterizing wave form distortion. In the (001) plane, the measurements show that the longitudinal velocity wave forms develop rarefaction shocks along $[100]$ and compression shocks along 26° from $[100]$. In the (110) plane, compression shocks are observed in the longitudinal velocity wave forms in the direction 37° from $[100]$, whereas rarefaction shocks are seen along $[1\overline{1}0]$. The results in the (001) and (110) planes are consistent with sign changes in the nonlinearity matrix elements. In the (111) plane, the measured wave form distortion is consistent with the phase changes associated with the computed complex-valued matrix elements. In particular, the characteristics of propagation in the $[11\overline{2}]$ and $[\overline{1}\overline{1}2]$ directions are shown to differ. This specific case is proved to follow from a more general result based on the symmetry properties of surface acoustic waves in this plane. In all the planes, it is demonstrated that, unlike bulk waves, the peak acoustic amplitude of surface waves can increase as they propagate, thereby allowing large stresses to be generated at surfaces. Finally, the power flux and total power of the pulses are shown to be substantially higher than in previous reports.

DOI: 10.1103/PhysRevB.69.035314 PACS number(s): 68.35.Iv, 62.65.+k, 43.25.+y, 43.35.+d

I. INTRODUCTION

Understanding the nonlinear properties of surface waves in crystalline materials is important for many applications. Piezoelectric surface acoustic wave (SAW) devices like convolvers, correlators, and amplifiers use nonlinear effects to perform signal processing functions. Many of these components are used in mobile and wireless communication devices for personal communication services (e.g., pagers, cellular phones), wide-area networks, and wireless local area networks.[1] SAW's have also been used to perform nondestructive evaluation (NDE). Defects, material properties (density, elastic constants), applied and residual stresses, adhesive bonding, surface roughness, and plate and layer thickness may all be measured using linear SAW's,[2] and the use of nonlinear SAW's to characterize materials — e.g., their fracture behavior — is a subject of current research.

Until the mid-1990s, much of the experimental work on nonlinear SAW's in crystals was limited to measurements of the first few harmonics. In 1996, Lomonosov and Hess[3] presented results of pulsed SAW's generated using an absorption-layer technique. Unlike previous experiments, this technique generates extremely high-amplitude pulses (peak strains approaching 0.01) with broadband spectra and allows the same pulse to be measured at multiple locations. Their original article showed wave forms in fused quartz that clearly exhibit shock formation. Additional wave forms in fused quartz were subsequently presented.[4,5] Comparison of those wave forms to the theory of Zabolotskaya and co-workers[6,7] for isotropic materials exhibited excellent quantitative agreement. Nonlinear surface wave pulses have also been excited in isotropic (polycrystalline) aluminum, copper, and stainless steel samples.[8–10]

Experiments have also been performed by Lomonosov and Hess in crystalline silicon. In the $[11\overline{2}]$ direction of the (111) plane, the measured pulse data[11] and the theory for anisotropic media[12] agreed well. Strikingly, it was found[13] in the (001) plane that the pulses distort in opposite ways, with longitudinal velocity wave forms forming rarefaction shocks in the $[100]$ direction and compression shocks in the direction 26° from $[100]$. (A compression shock is defined such that the longitudinal particle velocity is negative ahead of the shock and positive behind the shock; a rarefaction shock is the opposite case.) The same effects are predicted by theory,[12] which reproduces the wave form evolution in both directions. For a couple of the propagation directions described in Refs. 11 and 13, some additional measurements[3] have been presented, but a simplified, approximate theory was used to model those results.

The present article provides measured data in more cuts and directions than previous articles, with higher time resolution and more detailed analysis. The results corroborate previous theoretical investigations[14,15] of nonlinear surface waves in cubic crystals.

Finally, we note that measurements have also been made of finite-amplitude SAW's in systems of fused quartz substrates covered with titanium nitride films, and good agreement has been obtained with simulations.[16,17] However, because SAW's in these systems are dispersive, the resulting wave form evolution is qualitatively different than that presented here (e.g., shocks do not form). In addition, finite-

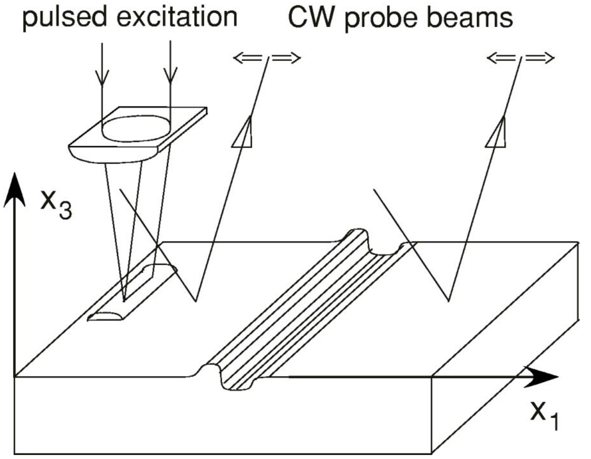

FIG. 1. Schematic diagram of the experimental apparatus using the absorption-layer method for finite-amplitude SAW generation and dual laser-probe SAW detection.

amplitude wave forms in silicon[18] have been published in which the excitation has been so large that fracture has occurred. These results extend beyond the range of the theory[12] for elastic waves used in this article.

II. EXPERIMENT

A schematic diagram of the experimental setup is shown in Fig. 1. Excitation of the SAW's is accomplished using a Nd:YAG laser of wavelength 1064 nm, pulse duration 8 ns, and energy up to 60 mJ, which is focused into a strip of length 7 mm and width 50 μm on the surface of the solid. This geometry creates a SAW beam which propagates outward from the the excitation region. A strongly absorbing layer in the form of an aqueous suspension of carbon particles is placed in the strip area. By explosive evaporation of this layer strong forces are exerted onto the surface, thereby intensifying the SAW excitation process. The nearly complete absorption of the laser pulse by the layer protects the surface from melting and ablation. To measure the transient SAW wave forms, a laser probe beam deflection setup using stabilized cw Nd:YAG laser probes of wavelength 532 nm and power 100 mW is employed. Two probe beams are focused into spots approximately 4 μm in diameter located 16 mm apart, with the closest probe between 0 and 5 mm from the excitation region. As the SAW pulse passes through the area covered by the probe beams, the deflection of the laser beams is detected by two position-sensitive detectors. Because the deflection of the beam is proportional to the slope of the surface, it follows that the detector output is proportional to the vertical velocity component of the traveling wave. The bandwidth of the whole detection system is limited to about 500 MHz.

III. SIMULATIONS

Numerical simulations are performed to compare theory and experiment for the three different data sets taken in crystalline silicon. In the theoretical description[12] of the wave forms on the surface, the particle velocity components are assumed to be plane waves expanded as follows:

$$v_j(x,\tau)=\sum_{n=1}^{\infty} A_n(x)B_j e^{-in\omega\tau}+\text{c.c.}, \tag{1}$$

where $j=1,2,3=x,y,z$ with $x=x_1$ the coordinate along the direction of propagation and $z=x_3$ the coordinate normal to the surface and directed outwards (see Fig. 1), $\tau=t-x/c$ is the retarded time, c is the linear wave speed in the propagation direction, B_j are derived from the eigenvectors of the linear problem,[14] and ω is the fundamental angular frequency. This assumption has two implications. First, the signal must be periodic. In order to model pulses, they are assumed to repeat with a frequency $f_{\text{rep}}=2.5$ MHz in all cases considered. Second, the signal must have planar wave fronts. Hence the theory is applicable only if diffraction effects are negligible; i.e., the total propagation distance x is less than the characteristic Rayleigh distance x_R of the beam. The ratio of these two lengths is given by the dimensionless diffraction parameter $D=x/x_R=4xc/\pi f_{\text{peak}}d^2$, where d is the beam width at the source and f_{peak} is the frequency of the peak spectral amplitude. In all cases $D\ll 1$, and therefore the wave fronts are essentially planar in the regions of interest.

To perform the simulations, the frequency spectrum of the measured wave form at the probe beam location closest to the excitation region is computed from the time wave form, appropriately scaled, and used as the source condition for the spectral evolution equations[12]

$$\frac{dA_n}{dx}+\alpha_n A_n=-\frac{n^2\omega c_{44}}{2\rho c^4}\sum_{l+m=n}\text{sgn}(lm)\hat{S}_{lm(-n)}A_l A_m, \tag{2}$$

where A_n and α_n are the spectral amplitude and absorption coefficient of the nth harmonic and $\hat{S}_{lm}$ is the nonlinearity matrix. (Note that $\hat{S}_{lm}=-S_{lm}/c_{44}$, where S_{lm} is defined in Ref. 12. This new matrix[14] is introduced so that sign and dimensions of $\hat{S}_{lm}$ are consistent with the nonlinearity matrix previously introduced for isotropic media.[6]) Physically, the matrix element $\hat{S}_{lm}$ describes the coupling between the lth and mth harmonics to generate the nth harmonic. This matrix has the property[12] that

$$\hat{S}_{pl,pm}=\hat{S}_{lm}/p \tag{3}$$

for any nonzero integer p, and hence the character of nonlinear distortions for a wave with $f_{\text{peak}}=pf_{\text{rep}}$ usually can be qualitatively characterized by the first few elements.[14,15] The absorption terms are introduced *ad hoc* to maintain numerical stability as shocks develop in the wave forms. Assuming classical absorption due to viscosity and heat conduction[19] yields the quadratic frequency dependence $\alpha_n=n^2\alpha_1$. The absorption coefficient $\alpha_1=0.00025/x_0$ is selected so that the absorption length is substantially larger than the characteristic length scale x_0 (defined below) for nonlinear effects. Provided that this condition was satified, we found that variations in the absorption coefficient primarily affected the magnitude of the sharp cusped peaks near the shock fronts and had relatively little effect on the rest of the wave form.

Moreover, this selection is reasonable given that measurements of longitudinal and transverse elastic waves in crystalline silicon indicate that the absorption is low, typically 0.5–1.5 dB/cm in the frequency range 200–500 MHz.[20] All the remaining coefficients including the nonlinearity matrix elements are computed from fundamental material constants: density ($\rho = 2331$ kg/m^3), second-order elastic constants from Hearmon[21] ($c_{11} = 165$ GPa, $c_{12} = 64$ GPa, $c_{44} = 79.2$ GPa), and third-order elastic constants from McSkimin and Andreatch[22] ($d_{111} = -825$ GPa, $d_{112} = -451$ GPa, $d_{123} = -64$ GPa, $d_{144} = 12$ GPa, $d_{155} = -310$ GPa, $d_{456} = -64$ GPa). Nonlinear coupling to bulk wave modes has been shown to be negligible in all cases considered here.[23] The evolution equations are then integrated numerically using a fixed-step-size, fourth-order Runge-Kutta routine over the distance between the probe beams.

The resulting frequency spectra are reconstructed into time wave forms using Eq. (1) and compared with the measured wave form at the second probe beam location. The longitudinal velocity wave forms are computed from the vertical velocity wave forms using the linear transformation[14]

$$v_1(x,\tau) = \mathrm{Re}(B_1/B_3)v_3(x,\tau) - \mathrm{Im}(B_1/B_3)\mathcal{H}[v_3(x,\tau)], \tag{4}$$

where

$$\mathcal{H}[f(\tau)] = \frac{1}{\pi}\mathrm{Pr}\int_{-\infty}^{\infty}\frac{f(\tau')}{\tau'-\tau}\,d\tau' \tag{5}$$

defines the Hilbert transform. The computations are performed with $N = 1200$ harmonics (i.e., $1 \leqslant n \leqslant N$, with $A_{-n} = A_n^*$), although the wave forms are reconstructed by using only enough harmonics ($N = 200$–500) to match the time resolution of the measured data.

In each case a characteristic nonlinear length scale[12] $x_0 = 1/|\beta|\epsilon k$ is computed to determine the effect of the nonlinearity over the distance between the probe beams, where k is a characteristic wave number associated with the peak spectral component and ϵ is the characteristic acoustic strain (acoustic Mach number). In cases where shocks form, x_0 is an estimate of the shock formation distance.[14] The estimated nonlinearity coefficient[14] is given by $\beta = 4\hat{S}_{11}c_{44}/\rho c^2$. Note that because $\hat{S}_{11}$ can be complex valued, β can also be complex valued. Physically, complex-valued matrix elements $\hat{S}_{lm}$ mean that both the magnitude and phase of the harmonics are changed as the wave propagates.[15]

IV. RESULTS

A. Silicon in the (001) plane

Figure 2 shows that the nonlinearity matrix elements of SAW's in the (001) plane of Si divide into three distinct regions[14] based upon the angle θ between the propagation direction and [100]. The matrix elements are all real valued as a result of the mirror symmetry of this plane. In region I ($0° \leqslant \theta < 21°$), the nonlinearity matrix elements are negative. In simulations with initially monofrequency waves,[14] this condition results in the v_3 wave forms forming sharply cusped peaks and the v_1 wave forms developing rarefaction shocks. In region II ($21° < \theta < 32°$), the nonlinearity matrix elements are positive. Correspondingly, the v_3 wave forms form sharply cusped troughs and the v_1 wave forms develop compression shocks. In region III ($32° < \theta \leqslant 45°$), the nonlinearity matrix elements are negative like region I, but significantly weaker. Surface wave pulses are measured in the pure mode directions $\theta = 0°$ and $\theta = 28°$ (marked by circles in Fig. 2). Table I presents parameters associated with the data in these directions.

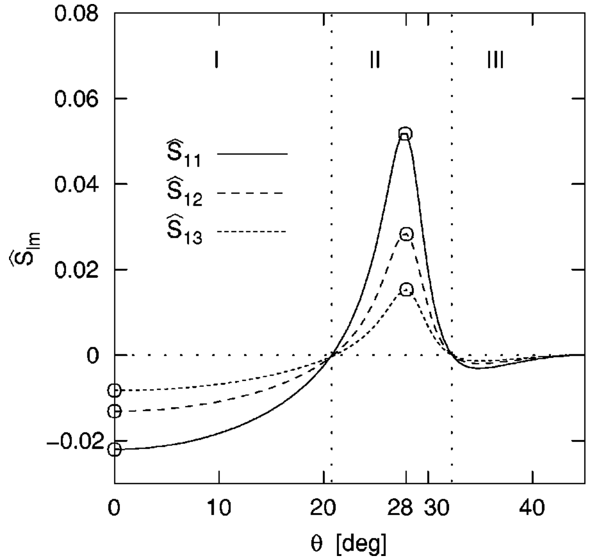

FIG. 2. Dependence of nonlinearity matrix elements on direction of propagation in the (001) plane in Si. The solid, long dashed, and short dashed lines correspond to $\hat{S}_{11}$, $\hat{S}_{12}$, and $\hat{S}_{13}$, respectively. Due to the symmetries of this cut, the matrix elements are symmetric about 45° and periodic every 90°. The circles indicate the directions of propagation considered in Figs. 3 and 4.

Figure 3 shows a comparison of experiment and theory for $\theta = 0°$. Figure 3(a) gives the directly measured vertical velocity component v_3 while Fig. 3(b) gives the longitudinal velocity wave form v_1, calculated from the measured v_3 wave form via Eq. (4). The velocity components are scaled

TABLE I. Parameters for SAW pulses in the (001) plane of crystalline silicon.

Parameter	Direction from [100]	
θ	0°	28°
c	4902 m/s	4954 m/s
$\lvert B_1/B\rvert$	0.632	0.534
$\lvert B_2/B\rvert$	0.000	0.339
$\lvert B_3/B\rvert$	0.774	0.775
D	0.081	0.12
$\hat{S}_{11}$	-0.022	0.052
β	-0.12	0.29
ϵ	0.0016	0.0082
f_{peak}	25 MHz	17.5 MHz
x_0	150 mm	19 mm

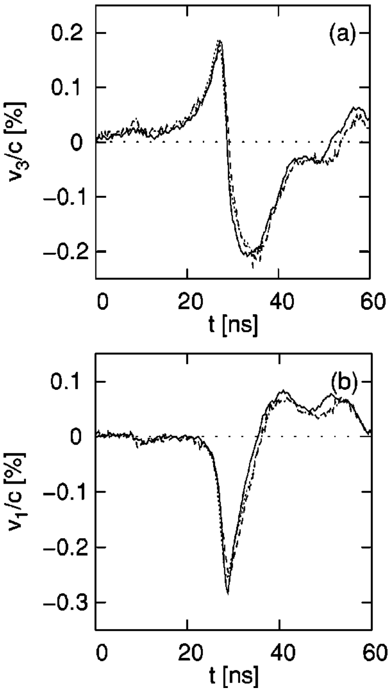

FIG. 3. Comparison of measured and simulated data for surface waves propagating in the direction [100] ($\theta=0°$) in the (001) plane of crystalline silicon, from $x=5$ mm (dashed line) to $x=21$ mm (solid line, measured; dotted line, simulated).

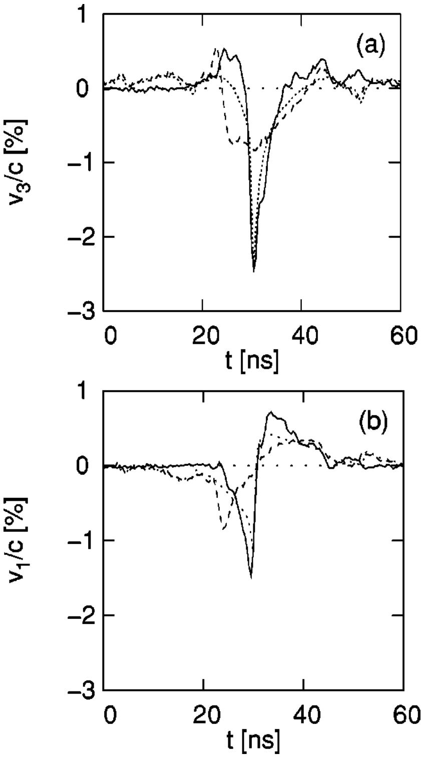

FIG. 4. Comparison of measured and simulated data for surface waves propagating in the direction $\theta=28°$ from [100] in the (001) plane of crystalline silicon, from $x=5$ mm (dashed line) to $x=21$ mm (solid line, measured; dotted line, simulated).

by the linear wave speed c in the direction of propagation because, as shown in Appendix A, the strain and stress components of the surface wave at the surface of the crystal are proportional to linear combinations of v_i/c. The dashed and solid lines give the experimental data for the close and remote probe beam locations from the source, and the dotted line gives the simulated result at the remote location. The wave has no transverse displacement component ($B_2=0$) in this direction. Because the propagation distance is much less than the estimated shock formation distance, the pulse only exhibits mild distortion. As seen in Fig. 2, the nonlinearity matrix elements are negative in this direction. As a result, the peaks of v_3 are expected to rise, and the troughs are expected to become flatter and shallower. In addition, the peaks of v_1 are expected to travel slower than the linear wave speed, and the troughs are expected to travel faster, with the result that rarefaction shocks form. Unfortunately, the weak distortion of the wave forms makes it difficult to determine if the predicted features are consistent with the observed evolution. However, this weakness itself is in agreement with the low magnitude of the nonlinearity matrix elements in this direction. In particular, the estimated shock formation distance is nearly an order of magnitude greater than the propagation distance.

In contrast, the magnitudes of the nonlinearity matrix elements are significantly larger in the direction $\theta=28°$. Figure 4 shows a comparison of the experiment with theory for this case. Unlike the $\theta=0°$ direction, the particle motion is tilted out of the sagittal plane. The resulting transverse velocity (shear horizontal) component is not qualitatively different from v_1, and while included in the full computations, its graph is omitted here. In this direction, the nonlinearity matrix elements are positive. Hence the peaks in v_1 travel faster than the linear wave speed, the troughs travel slower, and compression shocks form. The troughs of v_3 deepen and the peaks become flatter and shallower. Both of these features are clearly seen in the wave forms of Figs. 4(a) and 4(b). Note that while the wave forms measured at the close locations in the 0° and 28° directions are initially similar in form, they evolve to wave forms that are different. The resulting distortion in both cases is consistent with the regions of negative and positive nonlinearity delineated in Fig. 2.

Figure 5 shows the strain wave forms corresponding to the velocity wave forms in Fig. 4. (See Appendix A for analytical formulas for the strains and stresses.) Only the e_{11}, e_{33}, and e_{12} components are nonzero in this direction. The shape of the wave forms is similar to v_1 in all cases, although the e_{11} and e_{12} wave forms are inverted. As might be expected, the shear horizontal strain e_{12} arises mainly from the transverse velocity component, and waves without transverse components (e.g., the previous case along [100]) have no shear strain component. Note that the peak strains are a few percent, but only act over a period of around a nanosecond. Figure 6 shows the corresponding stress wave forms at the surface. Because of the stress-free boundary conditions, only the σ_{11}, σ_{22}, and σ_{12} components are nonzero. The primary effect of the wave is a rapid longitudinal compressional stress followed by a smaller (but still very large) tensile stress. The peak stress is several gigapascals, a value typical for the strongest excitations reported here. A

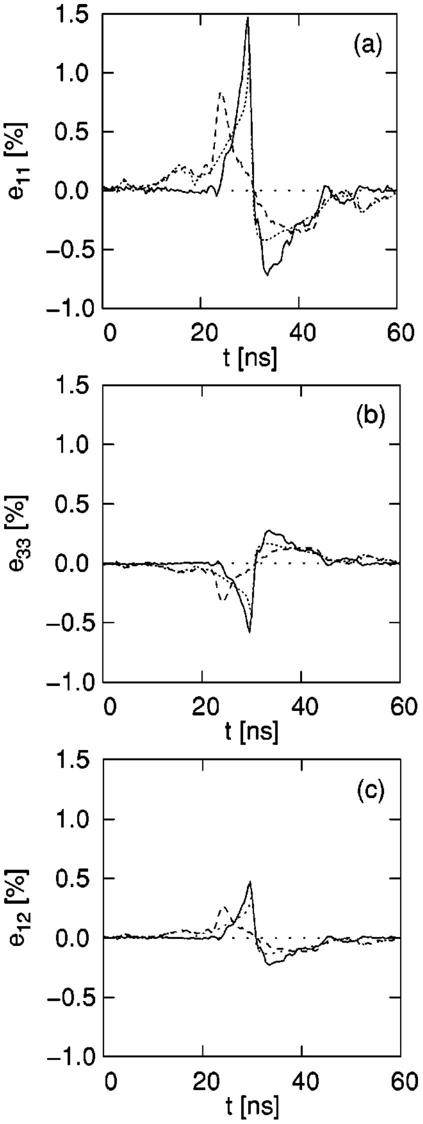

FIG. 5. Comparison of measured and simulated strain wave forms for surface waves propagating in the direction $\theta = 28°$ from [100] in the (001) plane of crystalline silicon, from $x = 5$ mm (dashed line) to $x = 21$ mm (solid line, measured; dotted line, simulated). Positive values of strain are compressive, while negative values are tensile. Only the nonzero components of strain are shown.

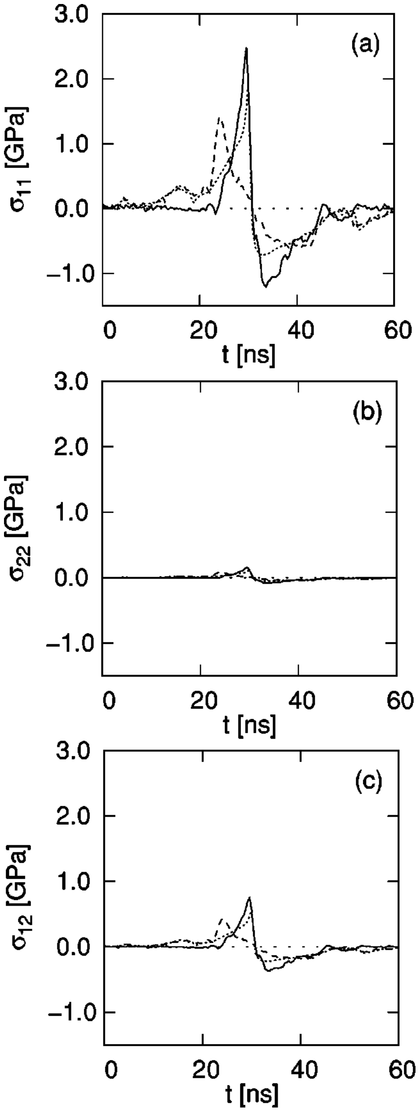

FIG. 6. Comparison of measured and simulated stress wave forms for surface waves propagating in the direction $\theta = 28°$ from [100] in the (001) plane of crystalline silicon, from $x = 5$ mm (dashed line) to $x = 21$ mm (solid line, measured; dotted line, simulated). Positive values of stress are compressive, while negative values are tensile. The remaining stress components are identically zero by the surface boundary conditions.

sizable shear horizontal stress exists because of the significant transverse velocity component in this case. In both the strain and stress wave forms it is clear that the peak amplitude increases as the wave propagates, an effect that is not seen in nonlinear bulk waves. Because it is relatively straightforward to compute the strains and stresses from the velocity components, we omit these graphs for the other cuts and directions that follow.

B. Silicon in the (110) plane

Next consider propagation in the (110) plane of Si. Surface wave pulses are measured in the pure mode directions $\theta = 0°$, 37°, and 90°, where in this section θ is defined as the angle between the propagation direction and [001]. The nonlinearity matrix elements for this cut are shown in Fig. 7, and the propagation directions are marked by circles. The nonlinearity matrix divides into regions of mixed sign, positive, and negative real-valued elements. Table II presents parameters associated with the data in these directions.

Figure 8 shows a comparison of experiment and theory for $\theta = 0°$. The wave has no transverse displacement component ($B_2 = 0$) in this direction. The nonlinearity matrix elements have mixed sign in this direction with $\hat{S}_{11} > 0$, $\hat{S}_{12} > 0$, and $\hat{S}_{13} < 0$. In simulations with initially monofrequency waves,[24] distortion occurs but shocks do not form because the various harmonic components change in opposite ways. With a pulsed wave form, the net effect appears to

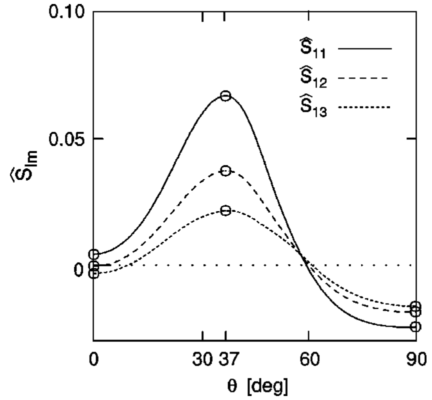

FIG. 7. Dependence of nonlinearity matrix elements on direction of propagation in the (110) plane in Si. The solid, long dashed, and short dashed lines correspond to $\hat{S}_{11}$, $\hat{S}_{12}$, and $\hat{S}_{13}$, respectively. Due to the symmetries of this cut, the matrix elements are symmetric about 90° and periodic every 180°. The circles indicate the directions of propagation considered in Figs. 8, 9, and 10.

be little distortion at all. Note that the nonlinearity matrix elements are typically an order of magnitude smaller in this direction than in the $\theta = 37°$ direction.

Figure 9 shows a comparison of experiment and theory for $\theta = 37°$. In this direction, the nonlinearity matrix elements are positive, and so the distortion is qualitatively very similar to Fig. 4. The similarity between these figures shows that the physical mechanism for the wave form distortion is the same in these directions despite being in different cuts.

Figure 10 shows a comparison of experiment and theory for $\theta = 90°$. In contrast, here the nonlinearity matrix elements are negative, and the distortion is qualitatively similar to Fig. 3. Note that the amplitude of the wave in this direction is less than the $\theta = 0°$ direction of this plane and yet the wave form exhibits more distortion. This result is consistent with the magnitudes of the nonlinearity matrix elements shown in Fig. 7 for the two different directions.

C. Silicon in the (111) plane

Finally consider propagation in the (111) plane of Si. Figure 11 shows the complex-valued nonlinearity matrix elements as a function of the angle θ between the propagation direction and $[11\bar{2}]$. Figure 11(a) shows that the effect of nonlinearity is near its maximum at $\theta = 0°$ and $\theta = 60°$ and weakest at $\theta = 30°$. While the magnitudes of the nonlinearity matrix elements have a sixfold symmetry in this cut, the phases have only a threefold symmetry. This property is general for SAW's propagating in this cut. (See Appendix B for a detailed discussion of the symmetry properties of linear and nonlinear parameters.) Note also that the magnitudes of the nonlinearity matrix element $|\hat{S}_{11}|$ (and hence nonlinearity coefficient $|\beta|$) are several times larger than those in the 0° and 26° directions of the (001) plane. Figure 11(b) shows that at $\theta = 0°$ the phases of the first few nonlinearity matrix elements are in the vicinity of 0.6π and are relatively close together. At $\theta = 30°$ the nonlinearity matrix elements are negative real valued, but as $\theta \rightarrow 60°$ the matrix elements approach $1.4\pi \equiv -0.6\pi \pmod{2\pi}$. As demonstrated for monofrequency source conditions,[15,25] the complex-valued nonlinearity results in an asymmetric distortion of the wave forms. For example, for $\theta = 0°$, the regions of the v_3 wave form from troughs to peaks steepen into a sharply cusped peak, while regions from peaks to troughs flatten, resulting in an N-shaped distortion. For v_1, the peaks rise into cusped spikes while the troughs become flatter and shallower, resulting in a U-shaped distortion. This combination of heightened nonlinearity and asymmetric distortion results in significantly different wave forms than observed in the (001) plane. Table III summarizes the relevant parameters for the SAW data in this cut.

TABLE II. Parameters for SAW pulses in the (110) plane of crystalline silicon.

Parameter	Direction from [001]		
θ	0°	37°	90°
c	5015 m/s	4784 m/s	4458 m/s
$\|B_1/B\|$	0.638	0.546	0.497
$\|B_2/B\|$	0.000	0.024	0.000
$\|B_3/B\|$	0.770	0.838	0.867
D	0.064	0.053	0.15
$\hat{S}_{11}$	0.0043	0.067	−0.025
β	0.023	0.40	−0.17
ϵ	0.0047	0.0085	0.0021
f_{peak}	32.5 MHz	37.5 MHz	12.5 MHz
x_0	220 mm	6.0 mm	160 mm

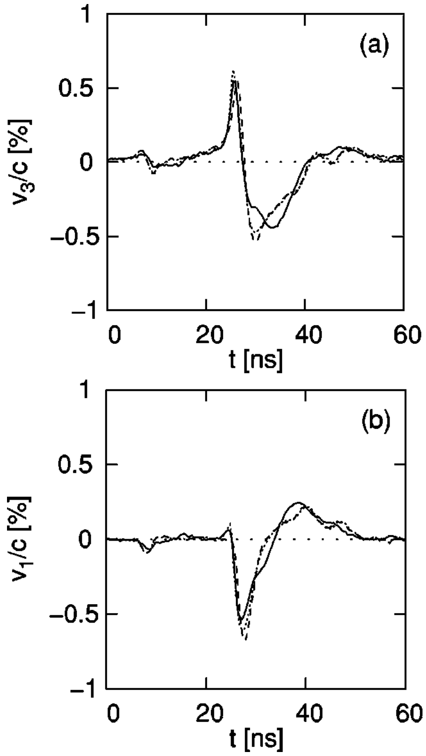

FIG. 8. Comparison of measured and simulated data for surface waves propagating in the direction [001] ($\theta = 0°$) in the (110) plane of crystalline silicon, from $x = 5$ mm (dashed line) to $x = 21$ mm (solid line, measured; dotted line, simulated).

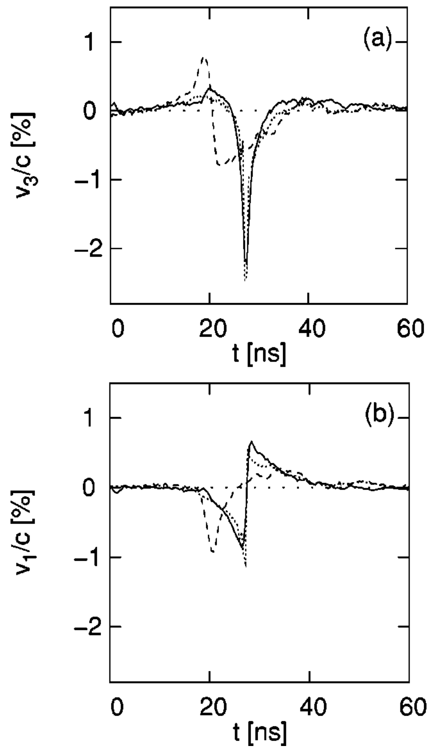

FIG. 9. Comparison of measured and simulated data for surface waves propagating in the direction $\theta = 37°$ from [001] in the (110) plane of crystalline silicon, from $x = 5$ mm (dashed line) to $x = 21$ mm (solid line, measured; dotted line, simulated).

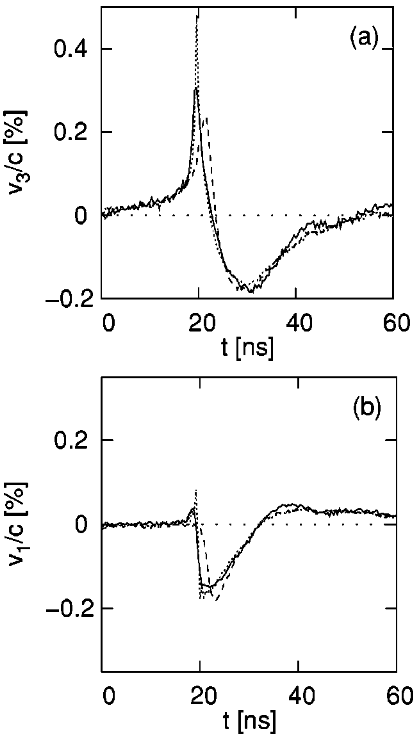

FIG. 10. Comparison of measured and simulated data for surface waves propagating in the direction $[1\bar{1}0]$ ($\theta = 90°$) in the (110) plane of crystalline silicon, from $x = 5$ mm (dashed line) to $x = 21$ mm (solid line, measured; dotted line, simulated).

Figure 12 provides a comparison of experiment with theory for $\theta = 0°$. In this particular direction, the wave has no transverse velocity component ($B_2 = 0$), and hence only the vertical and longitudinal components are shown in the Figs. 12(a) and 12(b). The nonlinear evolution (from the dashed line to the solid line) is predicted accurately by the theory (dotted line), including the increase in pulse duration between the close and remote locations. In Fig. 12, v_3 clearly has an N-shaped wave form while v_1 has a U-shaped wave form, as described previously. Figure 13 shows the spectra corresponding to Fig. 12. The top graph shows the measured spectrum at the first probe location, while the bottom graph shows the measured and simulated spectra at the second probe location in good agreement. Observe that the pulse lengthening seen in Fig. 12 is manifest in the shift of the spectral peak to a lower value between the first and second probe locations. In addition, the strongly nonlinear nature of the propagation is seen in the substantial increase in the amplitudes of harmonics.

Figure 13 also shows some features that are typical for all the measured spectra. First, it demonstrates that the limit of detector sensitivity occurs around 500 MHz and justifies the use of this value as the upper limit for reconstructing the simulated wave forms. Second, it shows that the bandwidth of the starting wave form is essentially narrower than the detector bandwidth, and so no higher harmonics are lost between the generation region and the first probe location. Finally, the spectra also indicate that the amplitude at f_{peak} is about 10 dB greater than the lowest-frequency components, and hence diffraction effects from these components are expected to be negligible.

In contrast to Fig. 12, Fig. 14 shows measured and computed results for $\theta = 30°$, where the nonlinearity matrix elements are negative real valued, like [100] in the (001) plane and $[1\bar{1}0]$ in the (110) plane. In this case, the peak of the v_3 wave form nearly doubles in size and the trough decreases slightly, while a rarefaction shock forms in the v_1 wave form. The velocity component v_1 is smaller than v_3 because in this case the wave also has a transverse component (not shown). Note also that the type of distortion in this direction is consistent with the other cases of negative real-valued nonlinear matrix elements seen in Figs. 3 and 10. The amount of overall distortion is somewhat less than in the $\theta = 0°$ direction, as consistent with the lower magnitude of the nonlinearity matrix elements of Fig. 11.

Finally, Fig. 15 shows measured and computed results for $\theta = 60°$. Here the initial amplitude of the wave is less than in previous cases, so the distortion is not as strong. The magnitudes of the nonlinearity matrix elements in this direction are the same as with $\theta = 0°$ in this plane, but the phases are opposite in sign. The opposite phasing causes the regions of the v_3 wave form from troughs to peaks to flatten, while regions from peaks to troughs steepen into sharply cusped peaks, resulting in an inverted N-shaped distortion. For v_1, the peaks become rounder and shallower, while the troughs deepen into cusped spikes, resulting in an inverted U-shaped distortion. Unlike the wave forms in Fig. 14 for $\theta = 30°$, the

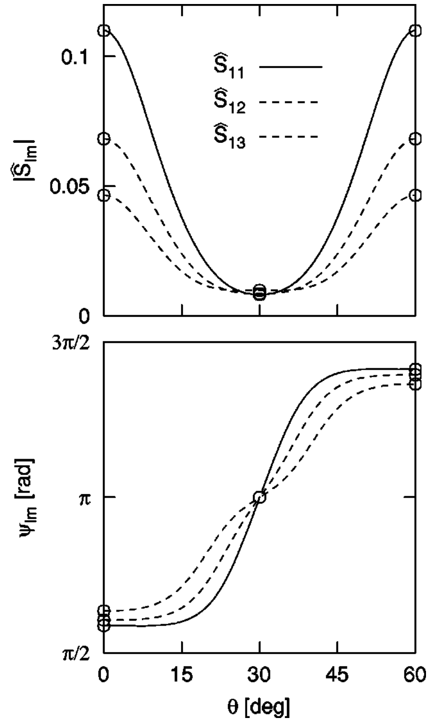

FIG. 11. Dependence of nonlinearity matrix elements on direction of propagation in the (111) plane in Si. The solid, long dashed, and short dashed lines correspond to $\hat{S}_{11}$, $\hat{S}_{12}$, and $\hat{S}_{13}$, respectively. The top plot shows the magnitudes $|S_{lm}|$, and the bottom plot shows the corresponding phase ψ_{lm}. Due to the symmetries of this cut, the matrix elements are symmetric about 60° and periodic every 120°. The circles indicate the directions of propagation considered in Figs. 12, 14, and 15.

v_3 wave form shows an increase in the the magnitude on both sides of the rarefaction shock and the trough of the v_1 wave form shows a substantial increase in magnitude. These results are consistent with those expected from simulations with initially monofrequency waves.[15]

The particle trajectory corresponding to the wave forms of Fig. 12 is shown in Fig. 16 at surface (largest), 24 μm below the surface (middle), and 60 μm below the surface (smallest and self-intersecting). Observe the very large vertical displacement caused by the wave (approximately 160 nm). In addition, the figure shows that the primary effect on the wave with increasing depth is the reduction in longitudinal motion.

TABLE III. Parameters for SAW pulses in the (111) plane of crystalline silicon.

Parameter	Direction from $[11\bar{2}]$		
θ	0°	30°	60°
c	4720 m/s	4522 m/s	4720 m/s
$\lvert B_1/B\rvert$	0.536	0.470	0.536
$\lvert B_2/B\rvert$	0.000	0.340	0.000
$\lvert B_3/B\rvert$	0.844	0.814	0.844
D	0.071	0.075	0.098
$\hat{S}_{11}$	$0.11e^{i0.59\pi}$	-0.0081	$0.11e^{-i0.59\pi}$
β	$0.65e^{i0.59\pi}$	-0.054	$0.65e^{-i0.59\pi}$
ϵ	0.0041	0.0028	0.0020
f_{peak}	27.5 MHz	25 MHz	19 MHz
x_0	9.7 mm	190 mm	30 mm

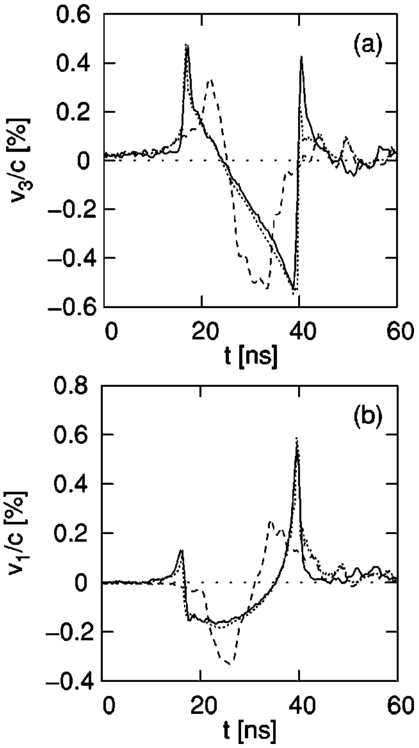

FIG. 12. Comparison of measured and simulated data for surface waves propagating in the direction $[11\bar{2}]$ ($\theta=0°$) in the (111) plane of crystalline silicon, from $x=5$ mm (dashed line) to $x=21$ mm (solid line, measured; dotted line, simulated).

D. Power flux

In the linear approximation, the energy carried by the surface wave consists of two parts: the potential energy of the elastic strain of the crystal and the kinetic energy associated with the motion of the material particles. Thus the total mechanical power per unit area in the x direction can be expressed as

$$E=c\left(\frac{1}{2}c_{ijkl}e_{ij}e_{kl}+\frac{\rho}{2}\frac{\partial u_i}{\partial t}\frac{\partial u_i}{\partial t}\right), \qquad (6)$$

where u_i are the displacement components and $e_{ij}=\frac{1}{2}(\partial u_i/\partial x_j+\partial u_j/\partial x_i)$ is the linearized strain tensor. Corrections to the power flow due to the elastic nonlinearity of the medium are cubic in the strain terms, which are limited to the order 10^{-2} by the mechanical strength of the solid.

Figure 17 shows $E(t)$ at the surface together with $F(t)$, the total power flow per unit length found by integrating $E(t)$ over depth. The two narrow peaks in $E(t)$ correspond to the shock fronts in the v_3 wave form of Fig. 12. Because higher-frequency components of the wave penetrate less deeply into the solid and because the shock fronts correspond to the high-frequency components, the acoustic energy of the pulse is more strongly confined near the surface at the shock fronts.

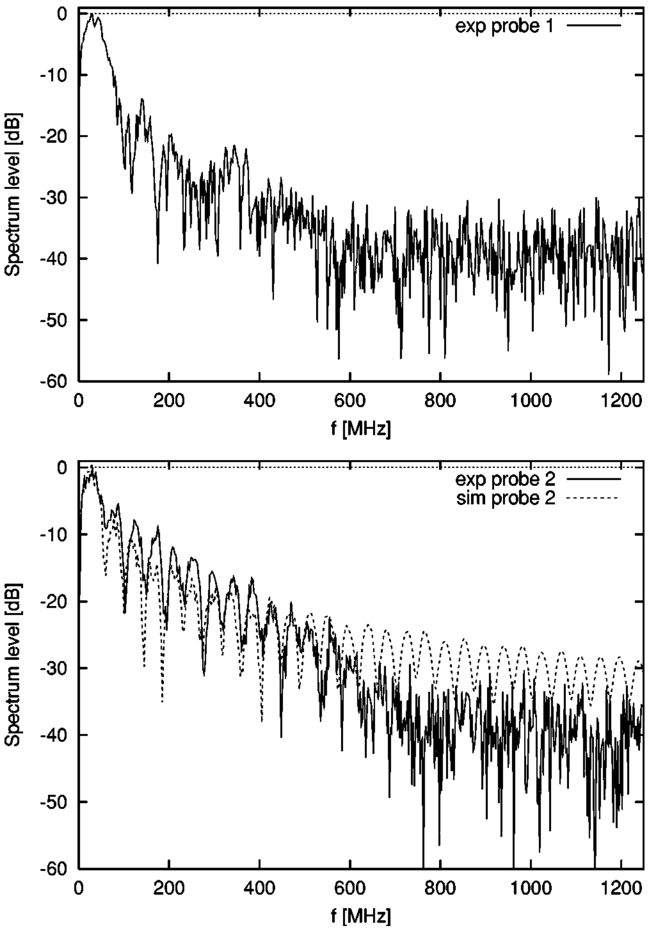

FIG. 13. Spectra for wave forms in Si in the direction $[11\overline{2}]$ ($\theta = 0°$) in the (111) plane. The top graph shows the measured spectra at the first probe location, while the bottom graph shows the measured (solid) and simulated (short dashed) spectra at the second probe location.

Integration over depth deemphasizes this confinement effect, so the peaks are considerably broader in $F(t)$. The minimum in $F(t)$ corresponds to the instant when the v_3 profile has zero value.

Additional interpretation of Fig. 17 can be obtained by examining the surface trajectory of Fig. 16. Because the motion of the wave is confined to the sagittal plane, $E(t)$ will have the quadratic form $k_1 v_1^2 + k_2 v_1 v_3 + k_3 v_3^2$. Figure 16 shows that the trajectory can be approximated by an ellipse with major axis nearly perpendicular to the surface, thereby making the cross term $k_2 v_1 v_3$ small. The magnitudes of the velocity components $|v_1|$ and $|v_3|$ are maximal where the longest horizontal and vertical components of the trajectory segments occur, respectively. Hence the maxima of $E(t) \approx k_1 v_1^2 + k_3 v_3^2$ will coincide with the maxima of $|v_1|$ and $|v_3|$. In this particular case, the first peak in Fig. 17 is formed almost solely by v_3 (17 – 19 ns). The second peak starts with its major contribution from v_3 (38 – 40 ns) but later v_1 dominates (40 – 42 ns). This transition from v_3 to v_1 in the second peak is more apparent in the plot of $F(t)$, where it appears as a local minimum between two maxima.

Table IV compares the values for the power flux and total power flow in Fig. 17 with those given in the previous publications.[26–31] In all these papers, the nonlinear effects were observed for an initially sinusoidal SAW which was generated by means of interdigital transducers on piezoelectric materials. (Note that the effective acoustic power is half the peak value for a sinusoidal source.) In comparison, the laser technique of SAW excitation provides substantially higher peak power density, a necessary condition for strong harmonic generation and shock formation to occur.

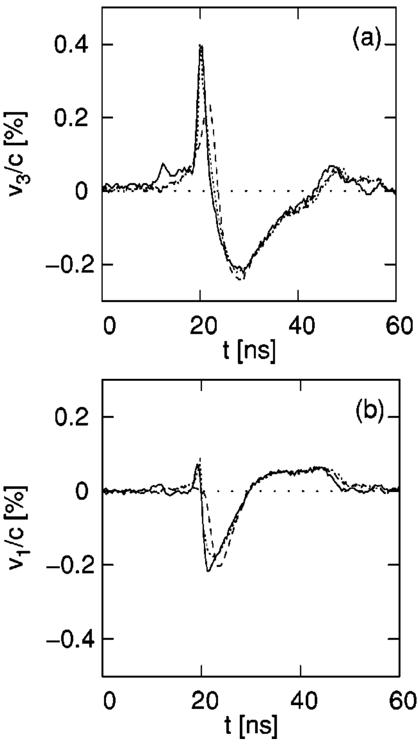

FIG. 14. Comparison of measured and simulated data for surface waves propagating in the direction [110] ($\theta = 30°$) in the (111) plane of crystalline silicon, from $x = 5$ mm (dashed line) to $x = 21$ mm (solid line, measured; dotted line, simulated).

V. CONCLUSION

This article investigates the propagation of nonlinear SAW pulses in crystalline silicon. Measurements are obtained for the directions 0° and 28° from [100] in the (001) plane, 37° and 90° from [001] in the (110) plane, and 0°, 30°, and $180° \equiv 60°$ (mod 120°) from $[11\overline{2}]$ in the (111) plane. The absorption-layer technique for the generation of nonlinear SAW's and the method used to numerically simulate the pulse propagation are described. In all cases, favorable agreement is achieved between experiment and theory. In the (001) and (110) planes, the pulses corroborate the predictions that there exist regions of directions with positive and negative nonlinearity. In the (111) plane, the wave form distortion is consistent with the phase changes associated with the complex-valued nonlinearity matrix elements. Unlike bulk waves, finite-amplitude SAW's in crystalline silicon are shown to often achieve peak acoustic amplitudes larger than their initial amplitude during

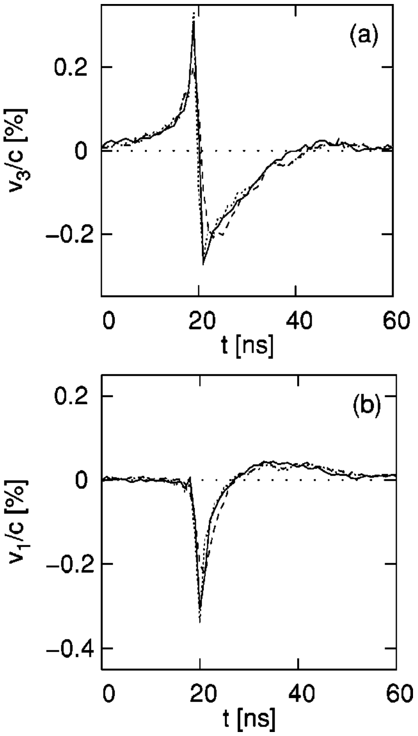

FIG. 15. Comparison of measured and simulated data for surface waves propagating in the direction $[\bar{1}\bar{1}2]$ ($\theta=180°\equiv60°$) in the (111) plane of crystalline silicon, from $x=5$ mm (dashed line) to $x=21$ mm (solid line, measured; dotted line, simulated). Note that the time resolution in this data is 1 ns as compared to 0.4 ns in Figs. 12 and 14.

propagation. This effect may be used to generate large-amplitude stresses near surfaces.

ACKNOWLEDGMENTS

This work was supported by the Deutsche Forschungsgemeinschaft, Russian Foundation for Basic Research, and U. S. Office of Naval Research. R.E.K. acknowledges support from the National Research Council, the National Institute of Standards and Technology, and the University of Windsor during the final preparation of this article. Discussions with Yu. A. Ilinskii, A. P. Mayer, and E. A. Zabolotskaya are also gratefully acknowledged.

APPENDIX A: STRAIN AND STRESS COMPONENTS

The velocity components of a nonlinear SAW are [Ref. 12, Eq. (74)]

$$v_j(x,z,t)=\sum_{n=1}^{\infty} A_n u_{nj}(z)e^{in(kx-\omega t)}+\text{c.c.}, \tag{A1}$$

where [Ref. 12, Eq. (27)]

$$u_{nj}(z)=\sum_{s=1}^{3}\beta_j^{(s)}e^{ink\zeta_s z}, \tag{A2}$$

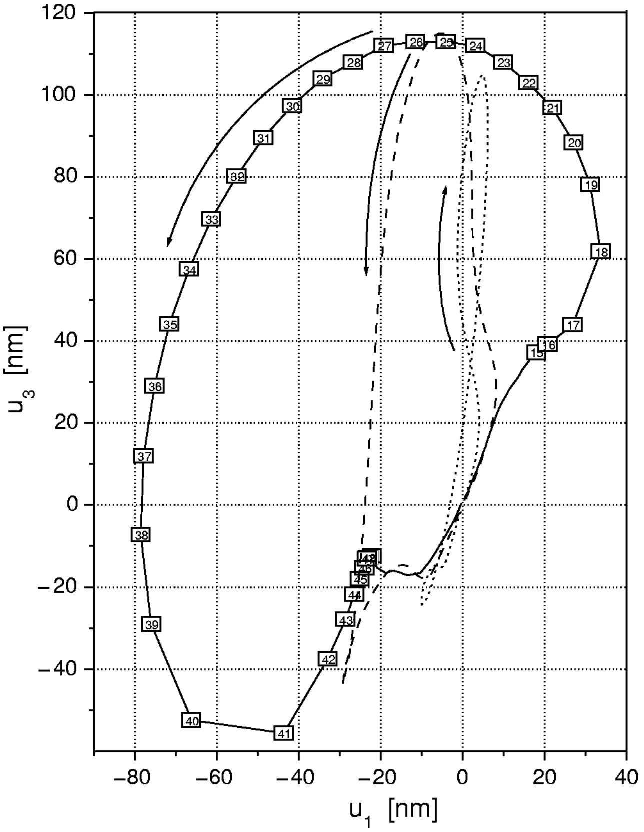

FIG. 16. Particle trajectory at the surface corresponding to the wave forms given in Fig. 12. The wave is traveling in the $[11\bar{2}]$ direction of the (111) plane. Trajectories are shown at 0 nm (solid line), 24 nm (dashed line), and 60 nm (dotted line) below the surface. The boxed numbers along the surface trajectory indicate the retarded time in nanoseconds.

and ζ_s and $\beta_j^{(s)}$ are associated with the eigenvalues and eigenvectors of the linearized SAW problem.[32] Note that these components are in the reference frame associated with the free surface and direction of propagation (x axis). By

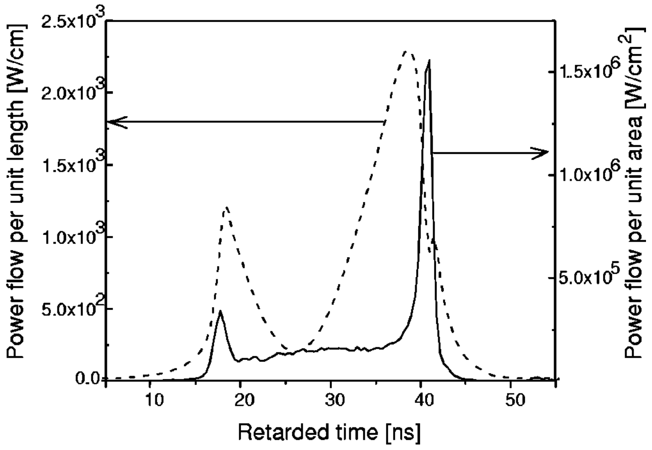

FIG. 17. Power flow per unit area $E(t)$ at the surface and power per unit length $F(t)$ normal to the direction of wave propagation. This measurement was taken at the remote location for the waveform in the $[11\bar{2}]$ direction in the (111) plane in Fig. 12.

TABLE IV. Comparison of power flow measurements in various SAW studies. When available, values are given for both power per unit area at the surface and power per unit length normal to the direction of wave propagation.

Authors	Material	W/cm^2	W/cm	Frequency [MHz]
Nakagawa *et al.*[a]	LiNbO$_3$	8×10^3	10	300
Gibson and Meijer[b]	SiO$_2$	N/A	2	281
Nayanov[c]	LiNbO$_3$	3×10^4	N/A	114
Cho and Miyagawa[d]	LiNbO$_3$	10^4	70	60
Kavalerov[e]	LiNbO$_3$	N/A	30	200
Kavalerov[f]	LiNbO$_3$	10^5	54	200
Current work	Si	1.5×10^6	2200	5 to 500

[a] Reference 26.
[b] Reference 27.
[c] Reference 28.
[d] Reference 29.
[e] Reference 30.
[f] Reference 31.

integration of Eq. (A1) with respect to time, it follows that

$$u_j(x,z,t)=\sum_{n=1}^{\infty}-\frac{1}{in\omega}A_n u_{nj}(z)e^{in(kx-\omega t)}+\text{c.c.} \quad \text{(A3)}$$

The strain components are

$$e_{ij}=\frac{1}{2}\left(\frac{\partial u_i}{\partial x_j}+\frac{\partial u_j}{\partial x_i}\right). \quad \text{(A4)}$$

The nonlinear contributions to the strain are not included in Eq. (A4) because, while they have a cumulative effect on the wave form evolution, they make only a small contribution at any individual location. Differentiating Eq. (A3) with respect each spatial variable yields

$$\partial u_j/\partial x=-v_j/c, \quad \text{(A5a)}$$

$$\partial u_j/\partial y=0, \quad \text{(A5b)}$$

$$\partial u_j/\partial z=-\hat{v}_j/c, \quad \text{(A5c)}$$

where

$$\hat{v}_j(x,z,t)=\sum_{n=1}^{\infty}A_n\hat{u}_{nj}(z)e^{in(kx-\omega t)}+\text{c.c.}, \quad \text{(A6)}$$

$$\hat{u}_{nj}(z)=\sum_{s=1}^{3}\zeta_s\beta_j^{(s)}e^{ink\zeta_s z}, \quad \text{(A7)}$$

and $\hat{u}_{nj}=\hat{u}^*_{(-n)j}$. The derivative dA_n/dx does not appear in Eq. (A5) because the relation $|dA_n/dx|\ll nk|A_n|$ is consistent with the nonlinear evolution equation (2). The individual strain components can then be computed using Eqs. (A5):

$$e_{11}=-v_x/c, \quad \text{(A8a)}$$

$$e_{22}=0, \quad \text{(A8b)}$$

$$e_{33}=-\hat{v}_z/c, \quad \text{(A8c)}$$

$$e_{23}=-\hat{v}_y/2c, \quad \text{(A8d)}$$

$$e_{13}=-(\hat{v}_x+v_z)/2c, \quad \text{(A8e)}$$

$$e_{12}=-v_y/2c. \quad \text{(A8f)}$$

Observe that e_{11} and e_{12} are always proportional the longitudinal and transverse velocity components scaled by the linear wave speed.

The stress components are

$$\sigma_{ij}=c_{ijkl}e_{kl}, \quad \text{(A9)}$$

where c_{ijkl} are the second-order elastic constants *defined in terms of the coordinate system associated with the free surface and direction of propagation*. Typically, the elastic constants are listed in reference books with respect to the crystalline axes, and hence to use Eq. (A9) a transformation of the stiffness matrix[33] is required for most propagation directions. Only the linear terms are included in Eq. (A9), for the same reasons as before with the strain. At the surface ($z=0$), the stress-free boundary conditions

$$\sigma_{13}=\sigma_{23}=\sigma_{33}=0 \quad \text{(A10)}$$

must hold. Substituting Eqs. (A8) and Eqs. (A10) into Eqs. (A9) yields

$$\hat{V}(z=0)=M_1^{-1}M_2V, \quad \text{(A11)}$$

where $\hat{V}=(\hat{v}_1\ \hat{v}_2\ \hat{v}_3)^T$, $V=(v_1\ v_2\ v_3)^T$,

$$M_1=\begin{pmatrix} c_{35} & c_{34} & c_{33} \\ c_{45} & c_{44} & c_{34} \\ c_{55} & c_{45} & c_{35} \end{pmatrix}, \quad \text{(A12a)}$$

$$M_2=\begin{pmatrix} -c_{13} & -c_{36} & -c_{35} \\ -c_{14} & -c_{46} & -c_{45} \\ -c_{15} & -c_{56} & -c_{55} \end{pmatrix}. \quad \text{(A12b)}$$

Hence at the surface, we find that $\hat{v}_j$, e_{ij}, and σ_{ij} can be written as a linear combination of the velocity components v_j, provided that $M_1^{-1}M_2$ is nonsingular.

As an example of this procedure, consider the special case of propagation in the (001) plane of a cubic crystal. In the crystalline frame, the only nonzero second-order elastic constants are[21] $c_{11}=c_{22}=c_{33}$, $c_{12}=c_{13}=c_{23}$, and $c_{44}=c_{55}=c_{66}$. In a frame rotated so that the x_1' axis is inclined at angle θ to the x_1 axis, the only constants which are changed by the rotation are[34]

$$c_{11}'=c_{22}'=c_{11}(\cos^4\theta+\sin^4\theta)+2(c_{12}+2c_{44})\sin^2\theta\cos^2\theta \quad \text{(A13a)}$$

$$c_{12}'=2(c_{11}-2c_{44})\sin^2\theta\cos^2\theta+c_{12}(\sin^4\theta+\cos^4\theta) \quad \text{(A13b)}$$

$$c'_{16}=-c'_{26}=(c_{11}-c_{12}-2c_{44})\sin\theta\cos\theta(\sin^2\theta-\cos^2\theta) \tag{A13c}$$

$$c'_{66}=4(c_{11}-c_{12})\sin^2\theta\cos^2\theta+c_{44}(1-8\sin^2\theta\cos^2\theta). \tag{A13d}$$

Note, however, that none of the second-order elastic constants in the matrices M_1 and M_2 of Eq. (A12) is affected by Eqs. (A13). Hence for all propagation directions it follows that

$$M_1^{-1}M_2=\begin{pmatrix} 0 & 0 & -1 \\ 0 & 0 & 0 \\ -c_{12}/c_{11} & 0 & 0 \end{pmatrix}. \tag{A14}$$

It immediately follows from Eq. (A11) that

$$\hat{v}_x^{z=0}=-v_z, \tag{A15a}$$

$$\hat{v}_y^{z=0}=0, \tag{A15b}$$

$$\hat{v}_z^{z=0}=-(c_{12}/c_{11})v_x. \tag{A15c}$$

After substituting Eqs. (A15) into Eqs. (A8), the only nonzero strains are

$$e_{11}^{z=0}=-v_x/c, \tag{A16a}$$

$$e_{33}^{z=0}=(c_{12}/c_{11})v_x/c, \tag{A16b}$$

$$e_{12}^{z=0}=-v_y/2c. \tag{A16c}$$

Substitution of Eqs. (A16) into Eqs. (A9) shows that the only nonzero stresses are

$$\sigma_{11}^{z=0}=\left(-c'_{11}+\frac{c_{12}^2}{c_{11}}\right)\frac{v_x}{c}-c'_{16}\frac{v_y}{c}, \tag{A17a}$$

$$\sigma_{22}^{z=0}=\left(-c'_{12}+\frac{c_{12}^2}{c_{11}}\right)\frac{v_x}{c}+c'_{16}\frac{v_y}{c}, \tag{A17b}$$

$$\sigma_{12}^{z=0}=-c'_{16}\frac{v_x}{c}-c'_{66}\frac{v_y}{c}. \tag{A17c}$$

Therefore, for propagation in the (001) plane it is sufficient to know the longitudinal and transverse velocity components to compute all the strains and stresses of the SAW at the surface. See Figs. 5 and 6 for graphs of the strains and stresses, respectively, for the case of $\theta=28°$. In the case of propagation along the crystalline axis,[35] $v_y=0$, $e_{12}=0$, $\sigma_{12}=0$, and only the longitudinal velocity component is necessary.

APPENDIX B: ASYMMETRY PROPERTIES OF SAWS IN CRYSTALS

Previous numerical and experimental studies of surface acoustic waves in the (111) plane of cubic crystals have shown that linear properties, including the wave speed and the direction of power flow, exhibit sixfold symmetry.[32] However, the measurements of Sec. IV C have demonstrated that the same periodicity does not hold for the nonlinear distortion. Calculations have indicated that complex-valued nonlinearity matrix elements as well as the complex-valued eigenvalues and eigenvectors of the linearized equations (physically corresponding to the depth decay coefficients and component amplitudes, respectively) have sixfold symmetry in magnitude but only threefold symmetry in phase.[36,15] It is shown here that such properties can be proved analytically to hold generally for SAW's in anisotropic media.

Consider first the linearized equation of motion for a surface acoustic wave. We assume a solution of the form $\exp[ik(\mathbf{l}\cdot\mathbf{x}-ct)]$, where $\mathbf{l}=(l_1,0,l_3)$. The secular equation is then

$$\det|c_{ijkl}l_jl_l-\rho c^2\delta_{ik}|=0. \tag{B1}$$

Equation (B1) can be split into four parts as follows:

$$\sum_{i+j=6}a_{ij}l_1^il_3^j+\sum_{i+j=4}b_{ij}l_1^il_3^j+\sum_{i+j=2}c_{ij}l_1^il_3^j-\rho^3c^6=0, \tag{B2}$$

where $i,j=0,\ldots,6$. We solve for l_3 and, in general, obtain three pairs of complex conjugate roots. Let q_1 and q_2 be a pair of such roots—i.e., $q_2=q_1^*$. The sextic secular equation can also be written in the general form

$$\sum_{n=0}^{6}K_nq^n=0, \tag{B3}$$

where q represents the roots for l_3. If we consider now the wave which travels in the opposite direction, then the l_1 component is replaced with $-l_1$. Analyzing Eq. (B2), we find that the terms with even powers of l_3 do not change their sign since they also contain even powers of l_1, whereas the terms with odd powers of l_3 do change their sign. So for the wave which is traveling in the opposite direction, Eq. (B3) transforms into the form

$$\sum_{n=0}^{6}(-1)^nK_nq^n=0. \tag{B4}$$

Thus, if $q_2=q_1^*$ satisfies Eq. (B3), then $-q_2=-q_1^*$ satisfies Eq. (B4). Because only the solutions with negative imaginary parts correspond to physical solutions (surface waves with amplitudes that decrease exponentially with depth), if l_3 is the solution for propagation in the direction x_3, then $-l_3$ must be the corresponding solution for propagation in the opposite direction. Hence, if l_3 contains a real part, the propagation becomes asymmetric about the origin in the plane. For the (111) plane of cubic crystals, this situation results in threefold directional symmetry instead of sixfold symmetry in the plane. Figures with calculated results for KCl have been given previously in Ref. 15.

The nonlinearity matrix elements can also be shown to have a similar asymmetry. Consider two waves v_1 and v_2 traveling in opposite directions—e.g., along the x_1 axis in positive and negative directions:

$$v^{(1)} = \sum_n V_n^{(1)} \exp(inkx), \tag{B5}$$

$$v^{(2)} = \sum_n V_n^{(2)} \exp(-inkx). \tag{B6}$$

If the waves have the same source condition, then $V_n^{(1)} = [V_n^{(2)}]^*$. Suppose the coefficients $V_n^{(1)}$ satisfy the evolution equation with nonlinearity matrix $S_{lm}^{(1)}$. The coefficients $V_n^{(2)}$ then satisfy the evolution equation with nonlinearity matrix $S_{lm}^{(2)} = [S_{lm}^{(1)}]^*$. Therefore, if the nonlinearity matrix elements contain an imaginary part, then the propagation will not be the same in opposite directions. This effect is exhibited in the (111) plane of silicon as can be seen by comparing Figs. 12 and 15.

---

*Current address: Department of Physics, University of Windsor, 401 Sunset Ave., Windsor, Ontario N3B 3P4, Canada. Electronic address: ronkumon@kumonweb.com

[1] C. Campbell, *Surface Acoustic Wave Devices for Mobile and Wireless Communication* (Academic Press, New York, 1998).

[2] *Ultrasonic Testing: Non-conventional Testing Techniques*, edited by J. Szilard (Wiley, New York, 1982).

[3] A. Lomonosov and P. Hess, in *Nonlinear Acoustics in Perspective*, edited by R. J. Wei (Nanjing University Press, Nanjing, China, 1996), pp. 106–111; A. Lomonosov and P. Hess, Phys. Rev. Lett. **83**, 3876 (1999).

[4] Al. A. Kolomenskii, A. M. Lomonosov, R. Kuschnereit, P. Hess, and V. E. Gusev, Phys. Rev. Lett. **79**, 1325 (1997).

[5] A. Lomonosov, V. G. Mikhalevich, P. Hess, E. Yu. Knight, M. F. Hamilton, and E. A. Zabolotskaya, J. Acoust. Soc. Am. **105**, 2093 (1999).

[6] E. A. Zabolotskaya, J. Acoust. Soc. Am. **91**, 2569 (1992).

[7] E. Yu. Knight, M. F. Hamilton, Yu. A. Il'inskii, and E. A. Zabolotskaya, J. Acoust. Soc. Am. **102**, 1402 (1997).

[8] A. A. Kolomenskii and H. A. Schuessler, Phys. Lett. A **280**, 157 (2001).

[9] Al. A. Kolomenskii and H. A. Schuessler, Phys. Rev. B **63**, 085413 (2001).

[10] Al. A. Kolomenskii, V. A. Lioubimov, S. N. Jerebtsov, and H. A. Schuessler, Rev. Sci. Instrum. **74**, 448 (2003).

[11] R. E. Kumon, M. F. Hamilton, Yu. A. Il'inskii, E. A. Zabolotskaya, P. Hess, A. Lomonosov, and V. G. Mikhalevich, in *Proceedings of the 16th International Congress on Acoustics and 135th Meeting of the Acoustical Society of America*, edited by P. K. Kuhl and L. A. Crum (Acoustical Society of America, Woodbury, NY, 1998), Vol. 3, pp. 1557–1558.

[12] M. F. Hamilton, Yu. A. Il'inskii, and E. A. Zabolotskaya, J. Acoust. Soc. Am. **105**, 639 (1999).

[13] R. E. Kumon, M. F. Hamilton, P. Hess, A. Lomonosov, and V. G. Mikhalevich, in *Nonlinear Acoustics at the Turn of the Millennium*, edited by W. Lauterborn and T. Kurz, AIP Conf. Proc. No. 524 (AIP, Melville, NY, 2000), pp. 265–268.

[14] R. E. Kumon and M. F. Hamilton, J. Acoust. Soc. Am. **111**, 2060 (2002).

[15] R. E. Kumon and M. F. Hamilton, J. Acoust. Soc. Am. **113**, 1293 (2003).

[16] A. M. Lomonosov, P. Hess, and A. P. Mayer, Phys. Rev. Lett. **88**, 076104 (2002).

[17] W.-S. Ohm, Ph.D. dissertation, The University of Texas at Austin, 2001.

[18] A. M. Lomonosov and P. Hess, Phys. Rev. Lett. **89**, 095501 (2002).

[19] R. W. Lardner, J. Appl. Phys. **55**, 3251 (1984).

[20] Yu. V. Ilisavskii and V. M. Sternin, Sov. Phys. Solid State **27**, 385 (1985).

[21] R. F. S. Hearmon, in *Elastic, Piezoelectric, Pyroelectric, Piezooptic, Electroptic Constants, and Nonlinear Dielectric Susceptibilities of Crystals*, edited by K.-H. Hellwege and A. M. Hellwege, Landolt-Börnstein, New Series, Group III, Vol. 11 (Springer-Verlag, New York, 1979), pp. 1–244.

[22] H. J. McSkimin and P. Andreatch, Jr., J. Appl. Phys. **35**, 3312 (1964).

[23] R. E. Kumon and M. F. Hamilton, J. Acoust. Soc. Am. **113**, 3060 (2003).

[24] R. E. Kumon, Ph.D. dissertation, The University of Texas at Austin, 1999.

[25] D. F. Parker and E. A. David, Int. J. Eng. Sci. **27**, 565 (1989).

[26] Y. Nakagawa, K. Yamanouchi, and K. Shibayama, J. Appl. Phys. **45**, 2817 (1974).

[27] J. W. Gibson and P. H. E. Meijer, J. Appl. Phys. **45**, 3288 (1974).

[28] V. I. Nayanov, JETP Lett. **44**, 314 (1986).

[29] Y. Cho and N. Miyagawa, Appl. Phys. Lett. **63**, 1188 (1993).

[30] V. Kavalerov, H. Katoh, N. Kasaya, M. Inoue, and T. Fujii, Jpn. J. Appl. Phys., Part 1 **34**, 2653 (1995).

[31] V. Kavalerov, N. Kasaya, M. Inoue, and T. Fujii, in *IEEE Ultrasonics Symposium Proceedings*, edited by M. Levy, S.C. Schneider, and B.R. McAvoy (IEEE, Piscataway, NJ, 1996), Vol. 2, pp. 839–844.

[32] G. W. Farnell, in *Physical Acoustics*, edited by W. P. Mason and R. N. Thurston (Academic, New York, 1970), Vol. 6, pp. 109–166.

[33] B. A. Auld, *Acoustic Fields and Waves in Solids*, 1st ed. (Wiley, New York, 1973), Vols. I and II.

[34] L. Gold, Phys. Rev. **104**, 1532 (1956).

[35] R. Stoneley, Proc. R. Soc. London, Ser. A **232**, 447 (1955).

[36] A. Lomonosov, P. Hess, R. E. Kumon, and M. F. Hamilton, J. Acoust. Soc. Am. **110**, 2702(A) (2001).